Towards Additive Manufactured Off-Earth Habitats with Functionally Graded Multi-Materials

Cheibas, Ina ; Laot, Mathilde; Rich, Belinda; Fu, Jia; Zhu, Jia-Ning; Popovich, Vera A.

DOI
10.1007/978-3-031-50081-7_4

Publication date
2024

Document Version
Final published version

Published in
Adaptive On- and Off-Earth Environments

Citation (APA)
Cheibas, I., Laot, M., Rich, B., Fu, J., Zhu, J.-N., & Popovich, V. A. (2024). Towards Additive Manufactured Off-Earth Habitats with Functionally Graded Multi-Materials. In A. Cervone, H. Bier, & A. Makaya (Eds.), *Adaptive On- and Off-Earth Environments* (pp. 59-89). (Springer Series in Adaptive Environments). Springer. https://doi.org/10.1007/978-3-031-50081-7_4

Chapter 4
Towards Additive Manufactured Off-Earth Habitats with Functionally Graded Multi-materials

Ina Cheibas, Mathilde Laot, Belinda Rich, Jia Fu, Jia-Ning Zhu, and Vera A. Popovich

Abstract This study investigated the feasibility of in-situ manufacturing of a functionally graded metallic-regolith multimaterial. To fabricate the gradient, digital light processing, an additive manufacturing technique, and spark plasma sintering were selected due to their compatibility with metallic-ceramic processing in a space environment. The chosen methods were initially assessed for their ability to effectively consolidate regolith alone, before progressing to sintering regolith directly onto metallic substrates. Optimised processing conditions based on the initial powder particle size, different compositions of the lunar regolith powders and sintering temperatures were identified. Experiments have successfully proven the consolidation of lunar regolith simulants first via near-net shaping with digital light processing and then spark plasma sintering at 1050 °C under 80 MPa. The metallic powders were fully densified at relatively low temperatures and a pressure of 50 MPa with spark plasma sintering. Furthermore, the lunar regolith and Ti_6Al_4V gradient were found to be the most promising multimaterial combination. While the current study showed that it is feasible to manufacture a functionally graded metallic-regolith, further developments of a fully optimised method have the potential to produce tailored, high-performance multimaterials in an off-earth manufacturing setting for the production of aerospace, robotic, or architectural components.

I. Cheibas (✉) · B. Rich
ESA/ESTEC European Space Agency, Noordwijk, The Netherlands
e-mail: cheibas@arch.ethz.ch

M. Laot · J. Fu · J.-N. Zhu · V. A. Popovich
Department of Materials Science and Engineering, Delft University of Technology, Delft, The Netherlands

A. Cervone et al. (eds.), *Adaptive On- and Off-Earth Environments*, Springer Series in Adaptive Environments, https://doi.org/10.1007/978-3-031-50081-7_4

4.1 Introduction

Lunar exploration is a strategic cornerstone for future space exploration missions (Benaroya 2018; Eckart 1999), the infrastructure of which will include space habitats and engineering tools. The space habitats concepts are generally classified as a container configuration or a hybrid structure with rigid and inflatable components (Benaroya 2022; Dronadula and Benaroya 2020). These structures have to guarantee high-mechanical performances in an indoor pressurised and controlled atmosphere to secure safety against the harsh space conditions (Howe and Sherwood 2009; Naser and Chehab 2018). Additionally, the fabrication method of such structures requires in-situ autonomous building capabilities, to diminish maintenance, payload volume from Earth, and increase habitat expandability (Frank et al. 2013; Higgins and Benaroya 2020). Therefore, the design of lunar space habitats and robotic exploration tools use in-situ resources as manufacturing proposals.

In-situ resource utilisation (ISRU) is a key strategy for manufacturing space habitats and instruments (Kennedy 2002; Sanders and Larson 2012; Nunn et al. 2022; Ellery 2022). The primary and most abundant ISRU material on the Moon is the lunar soil, also known as regolith. Regolith is an abrasive and corrosive powder that contains several silicates and oxide minerals, see Table 4.1 (Edmunson and Rickman 2012; Papike et al. 1982; Crawford 2015; Rasera et al. 2019). The silicates and oxide minerals are abundant in metals such as silicon (Si), aluminium (Al), iron (Fe), titanium (Ti), and magnesium (Mg) (Mueller et al. 1988; Pieters 1986; Prettyman et al. 2006; Taylor 1987). These metals can be extracted from the robotically drilled lunar soil through pyrometallurgy, electrometallurgy, or hydrometallurgy methods (Zhang et al. 2021a; Allen et al. 1996; Landis 2007; Ellery et al. 2022). Such industrial-scale production methods have been proven viable for electro-deoxidation of powdered lunar regolith simulants, with oxygen as a by-product in the refining process (Lomax et al. 2019). A significant potential of these processes can be through metal extraction through a reactive gas, reduction through electrolysis, vapour phase pyrolysis, or thermal extraction of volatiles and water ice (Schlüter and Cowley 2019).

Similar to Earth-based construction techniques, a lunar habitat can use metal for fabricating a thin structural shell or reinforcements for increased mechanical strength (Buchanan and Gardner 2018). Nevertheless, metallic powders have not yet been investigated for building a lunar habitat. Although, metal robotic fabrication has been proven for Earth applications (Kanyilmaz et al. 2021). For example, MX3D has built a 10.5 m span metal footbridge, while topology optimization became a generally adopted technique in metal robotic fabrication, to improve mechanical performance and decrease material usage, see Fig. 4.1 (Gardner et al. 2020; Galjaard et al. 2015).

Furthermore, current research focuses largely using only regolith simulant as a feedstock for space habitat additive manufacturing (Labeaga-Martínez et al. 2017; ASTM F2792–12 2012). Additive manufacturing (AM) methods are generally selected based on their technological feasibility for a lunar scenario and material performance (Dordlofva and Törlind 2017; Isachenkov et al. 2021). For example, vat

Table 4.1 Summary of mineralogical content (in wt.%) of three lunar regolith simulants (EAC-1A, LHS-1 and LMS-1) in comparison to the average volume percentages collected at the Apollo and Luna sites (Brown et al. 1975; Eckart et al. 1999)

	EAC-1A	LHS-1	LMS-1	Modal proportions
Plagioclase	17.0	74.4	19.8	12.9–69.1
Basaltic glass mare	–	–	32.0	0.9–17.2
Basaltic glass highlands	–	24.7	–	3.8–25.0
Ilmenite	–	0.4	4.3	0.0–12.8
Pyroxene	22.0	0.3	32.8	8.5–61.1
Olivine	14.0	0.3	11.1	0.2–17.5
Iron oxide	13.0	–	–	–
Other	8.0	–	–	–
Total	**74.0**	**100**	**100**	

Fig. 4.1 Robotic fabrication of the metal MX3D bridge (2021)

polymerization and digital light processing (DLP) are small-scale fabrication techniques that utilise light-activated polymer to produce high-fidelity parts, see Fig. 4.2a (Altun et al. 2020a; Carloni et al. 2021). These techniques proved the potential for ceramic-based slurries in microgravity (Dou et al. 2022). Material extrusion and binder jetting are the most common large-scale AM techniques that use water with regolith in a concrete slurry (Khoshnevis, et al. 2005; Pilehvar et al. 2020; Cesaretti et al. 2014). The disadvantage of this method is the large amounts of water, organic or chemical binders required, which highly scarce and valuable in an extraterrestrial setting or would need to be brought from Earth in large quantities. Furthermore, the vacuum and microgravity can alter the porosity, interface bonding, and mechanical strength of the materials in this process (Cheibas et al. 2022; Li et al. 2020; Cordonier et al. 2021). Other AM methods include laser sintering, solar sintering, and powder bed fusion (Kost et al. 2021; Fateri et al. 2014; Fateri and Gebhardt 2015; Goulas et al. 2017). The first solar 3D-printed brick, manufactured with lunar regolith simulant, has been demonstrated as a proof-of-concept, see Fig. 4.2b (Fateri et al. 2019; Meurisse et al. 2018). Alternative fabrication methods include microwave-sintering

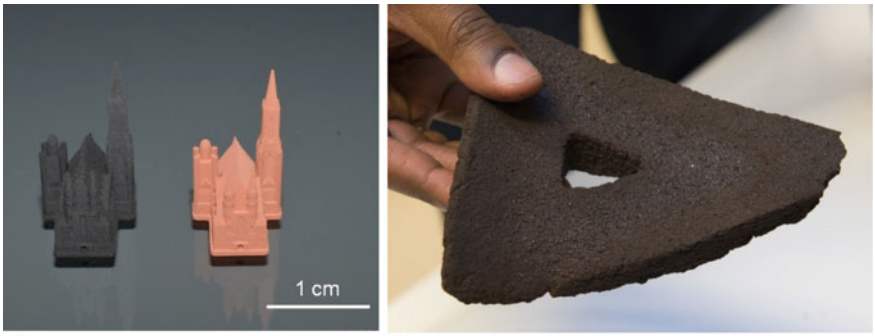

Fig. 4.2 **a** Vat polymerization of parts from lunar regolith simulant (Altun et al. 2020a); **b** 3D-printed brick from lunar regolith simulant using focused sunlight, European Space Agency (https://www.esa.int/ESA_Multimedia/Images/2017/03/Brick_3D_printed_from_moondust_using_focused_sunlight)

and spark plasma sintering (Kim et al. 2021). Spark plasma sintering is advantageous because the process can use vacuum, similar to the space environment, in the regolith densification process (Licheri et al. 2022; Zhang et al. 2019a).

Nevertheless, the vast majority of these fabrication studies have so far produced small-scale components with inadequate mechanical properties (Goulas et al. 2019; Lakhdar et al. 2021; Isachenkov et al. 2021). The results exhibit limited compressive or tensile strength, not yet adequate for a large-scale habitat structure (Cesaretti et al. 2014; Goulas et al. 2017; Goulas and Friel 2016; Meurisse et al. 2017; Neves et al. 2020; Heiken et al. 1991). Therefore, there is a need for resilient composites that can overcome all the harsh space conditions and take full advantage of the potential of ISRU.

Functionally graded materials (FGM) are high-performance composites designed to achieve tailored features (Bever and Duwez 1972). FGM can overcome the multitude of lunar requirements with functions or performance embodied in a graduated morphology. These materials are advantageous for maximising ISRU capabilities due to their multimaterial approach, which can provide high-performance relative to monolithic applications (Kim and Na 1995; Suresh and Mortensen 1997; Srivastava et al. 2019). FGM can improve mechanical behaviour via a specific distribution of materials in a graded layer. Several metal-ceramic gradients have been widely studied in recent years because of their attractive properties, such as high–temperature stability, high hardness, corrosion resistance, and versatility (Balla et al. 2007; Gong et al. 2018; Jin et al. 2018; Kamaruzaman et al. 2018; Katz-demyanetz et al. 2019; Maseko et al. 2018; Popovich et al. 2018; Guisard Restivo, et al. 2019; Zhang et al. 2018). A regolith to metal gradient could potentially be manufactured to combine ceramic-like properties with metal-like mechanical behaviour (Jin et al. 2018; Kamaruzaman et al. 2018; Liao et al. 2020). Such materials are expected to demonstrate improved resistance to thermal fatigue over conventional interfaces due to their graduated nature (Guisard Restivo

10 et al. 2019), a crucial requirement for the dramatic thermal cycles experienced on the lunar surface, as well as high overall fracture toughness due to the presence of intermediate metallic-ceramic phases (Rattanachan et al. 2003). Compressive strength is expected to be in line with other regolith consolidation methods, in the range of 2 to 10 MPa (Altun et al. 2020b).

This research investigated the automated fabrication feasibility of functionally graded multimaterials for a lunar habitat. The manufacturing technique plays an essential role in achieving such a gradient. Spark plasma sintering, a technique often used for metallurgical powder consolidation, has been previously investigated for regolith simulants and separately for FGM manufacture (Pasha and Rajaprakash 2021). Additionally, previous research investigated the powder characterisation of regolith simulants to determine the feasibility of using AM to produce FGMs (Cheibas et al. 2020). In this study, chemical composition, thermal characteristics, particle shape, and size distribution of the powders were analysed to determine regolith processability. Furthermore, it was found that digital light processing (DLP) and spark plasma sintering (SPS) are compatible consolidation techniques for both ceramic and metal powders, and thus for FGMs (Zhang et al. 2021b, 2019b; Liu et al. 2019; Balla et al. 2012). However, the preparation of the lunar simulant, particularly sieving and crushing, is necessary before consolidation due to the large particle size and shape.

4.2 Materials and Methods

4.2.1 Powder Characterisation

Three regolith simulants were evaluated for the manufacture of a functionally graded metallic-regolith: EAC-1A, Lunar Highlands Simulant (LHS-1), and Lunar Mare Simulant (LMS-1).

The EAC-1A simulant was sourced from the European Astronaut Centre, Cologne, Germany, while LHS-1 and LMS-1 simulants were sourced from the CLASS Exolith Lab, Orlando, USA (Cannon 2019). The use of simulant powders is necessary due to the limited availability of lunar soil. Thus, some differences between the terrestrial simulants and the actual lunar material are to be expected. Table 4.2 shows the similarity in oxide and mineralogical compositions between the chosen simulants and lunar Apollo samples. The element compositions of suite soils from the Apollo landing sites differ depending on the area of extraction: maria or highlands. The Apollo maria samples are similar to the LMS-1 simulant, with a higher concentration of titanium (Ti), ferrous oxides (FeO), and lower concentration of aluminum (Al). The highlands samples have a lower titanium (Ti) and iron (Fe) concentration, and higher aluminum in (Al) and calcium (Ca), similar to the LHS-1 simulant.

As seen in Table 4.1, the dominant mineralogical content in the simulants is plagioclase, pyroxene, and olivine, characteristics of basaltic composition. The lunar

Table 4.2 Oxide composition (given in wt.%) of three lunar regolith simulants (EAC-1A, LHS-1, and LMS-1 (Cannon 2019; Schleppi et al. 2019), and the average of the lunar surface samples from Apollo Maria and Highlands regions (Mueller et al. 1988; Sibille et al. 2006)

	EAC-1A	LHS-1	LMS-1	Apollo Maria	Apollo Highland
SiO_2	43.70	51.20	46.90	45.4	45.50
TiO_2	2.40	0.60	3.60	3.90	0.60
Al_2O_3	12.60	26.60	12.40	14.90	24.00
Fe_2O_3	12.00	–	–	–	–
FeO	–	2.70	8.60	14.10	5.90
MgO	11.90	1.60	16.80	9.20	7.50
MnO	0.20	0.10	0.20	–	–
CaO	10.80	12.80	7.00	11.80	15.90
Na_2O	2.90	2.90	1.70	0.60	0.60
K_2O	1.30	0.50	0.70	–	–
P_2O_5	–	0.10	0.20	–	–
Total	**98.40**	**99.40**	**99.00**	**99.9**	**100**

highlands are more chemically simplified than the mare basalts. The highlands have different textural relationships dependent upon the degree of melting and recombination with other mineralogical components. Moreover, essential differences exist between the Moon and Earth basalts. The key mineralogical difference in the lunar samples is the presence of Fe0 and Fe^{2+}, compared to terrestrial materials that typically consist of Fe^{2+} and Fe^{3+}.

Figure 4.3a shows the particle size distribution of each lunar simulant. All simulants exhibit a wide particle size range, namely, 0.02–2000 μm for EAC-1A and <1 μm–1000 μm for LHS-1 and LMS-1. The mean particle size is 10.5 μm for EAC-1A, 94 μm for LHS-1, and 63 μm for LMS-1 (Cannon 2019; Smith et al. 2018). The significant large grain fraction was predicted to cause difficulty in additive manufacturing, particularly in densification during sintering. Due to this, all three simulants underwent sieving through 50 or 100 μm mesh sieves to allow better sintering. A 30 g batch of EAC-1A was milled in a Retsch planetary ball mill in an argon atmosphere using tungsten carbide balls (5 and 10 mm). The powder was milled for 30 h at a speed of 300 rpm with a ball to powder mass ratio of 10:1. The contamination was kept very low, and the maximum particle size was reduced to 22 μm with mean particle size of 5 μm. Figure 4.3b shows X-ray diffraction (XRD) patterns for all three lunar regolith simulants and confirms the presence of plagioclase, pyroxene, and iron oxide.

To characterise the thermal behaviour of the given simulants, combined differential scanning calorimetry (DSC) and thermogravimetric analysis (TGA) were conducted (Cheibas et al. 2020). It was found that all three simulants exhibited a thermal transformation in the 1100–1500 °C temperature range, as shown in Fig. 4.4, consistent with the melting of basalt, ilmenite and glasses present in the simulants.

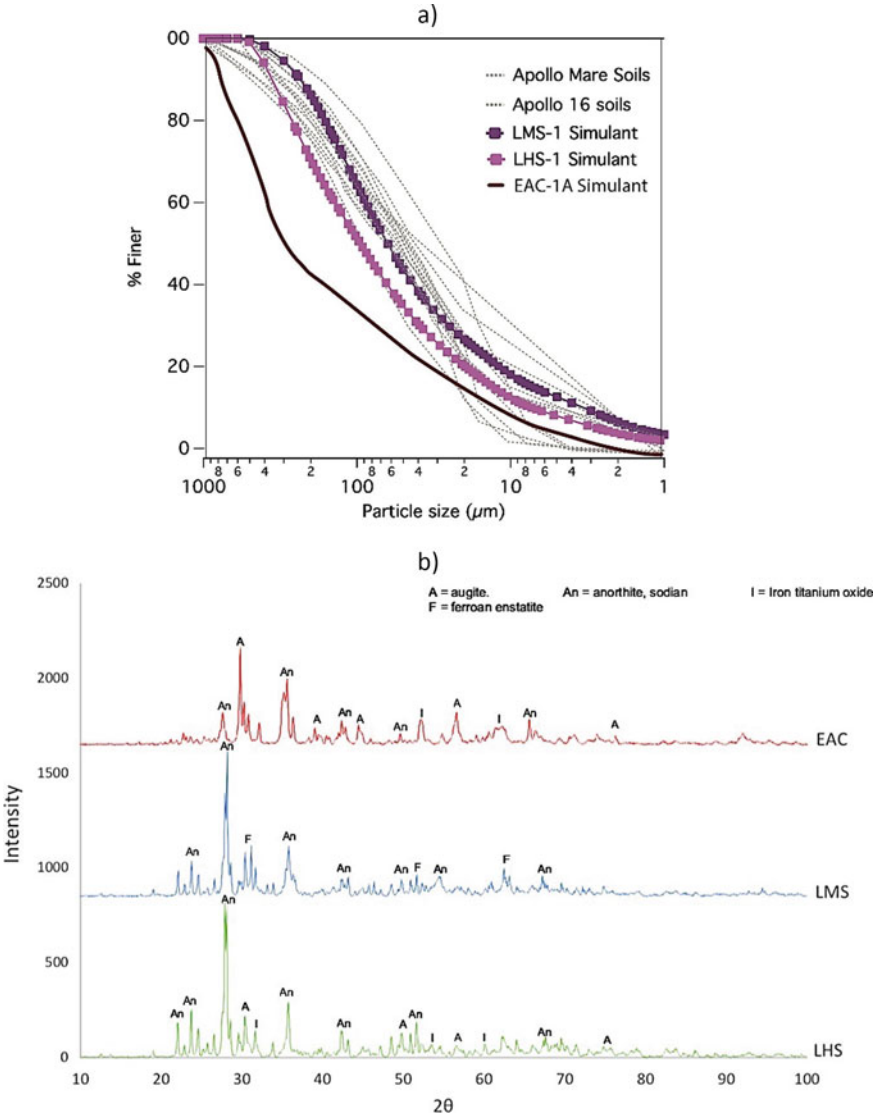

Fig. 4.3 **a** Average particle size distribution for EAC-1A, LHS-1 and LMS-1. Apollo data is shown for comparison, and has been adjusted to remove the >1 mm fraction; **b** XRD patterns of the 3 lunar regolith simulants powders (Cheibas et al. 2020).

This temperature range is also within the melt temperature range for plagioclase, especially high-Na content plagioclase, thus the exhibited thermal transformations can be attributed to the melting or partial melting of some mineralogical regolith constituents. Mass losses ranging from 0.97 to 2.75% were also observed in the simulants at temperatures above 1350 °C, which is attributed to the loss of volatiles

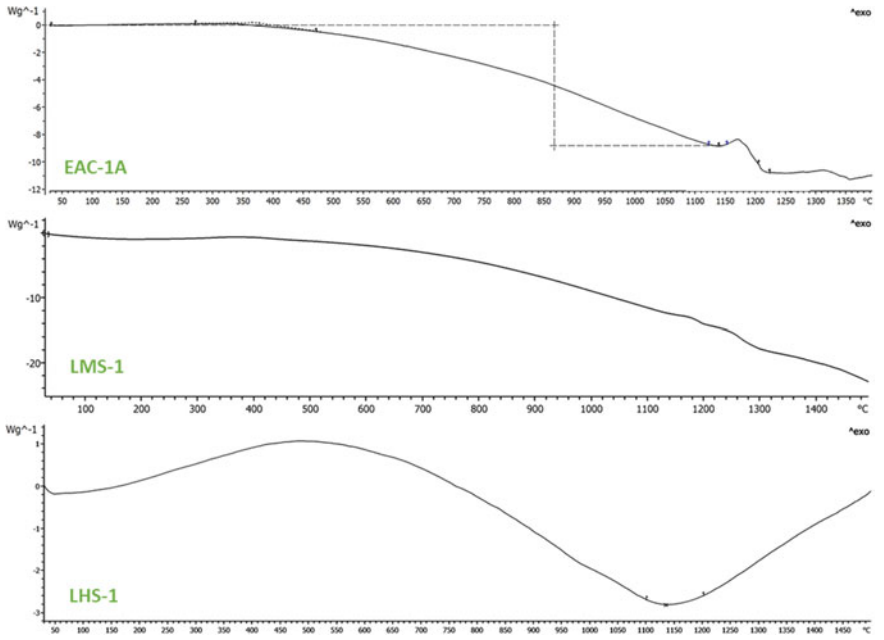

Fig. 4.4 Differential scanning calorimetry traces for lunar simulants EAC-1A (top), LMS-1 (centre) and LHS-1 (bottom)

from the powder, a behaviour that is not shared by regolith originating in the arid lunar environment. Care should be taken when conducting experiments with simulants to remove volatiles with an initial drying step.

Regarding metal, several elements such as titanium, iron, and aluminum are abundant in lunar soil. Pure metallic powders have the potential to be extracted on the Moon and used to fabricate FGM. However, this research is a first step to determine the feasibility of a functionally graded regolith-metallic substrate. Due to the novelty of this study, an investigation is necessary to determine if the interface between the regolith and a terrestrial AM metallic powder is possible. Stainless steel 316L and Ti_6Al_4V are high-grade metallic powders, frequently used in the aerospace industry for AM techniques (Geng et al. 2021; Mertens et al. 2014). These powders are selected because of their proven FGM potential and enhanced mechanical properties (Karami et al. 2020; Ruys et al. 2001). Therefore, in this study, the metallic powders used are stainless-steel 316L and Ti_6Al_4V. The stainless steel powder was provided by Admatec (Alkmaar, The Netherlands) with a particle size range of <1 to 30 μm. The powder contains mainly austenite with a small portion of ferrite. Ti_6Al_4V powder was provided by AP&C advanced powder and coatings, with a particle size range of 15–45 μm. The powder is composed solely of the alpha phase, an HCP lattice of Ti_6Al_4V.

4.2.2 Additive Manufacturing Consolidation Techniques

Stereolithography, laser powder bed fusion (L-PBF), and direct energy deposition (DED) are some of the AM methods able to process metal powders. However, the fabrication of functionally graded metallic-regolith has to be compatible with both the metal powders and lunar regolith. In the case of L-PBF and DED, the current hardware to control a robust graded multimaterial deposition is limited. Stereolithography, namely digital light processing (DLP), however, has the potential to achieve a metallic-regolith gradient and has been proven to work with lunar simulants (Altun et al. 2020b). Therefore, DLP has a higher probability of success in consolidating the regolith and FGM as a proof of concept.

The DLP method is a liquid-based AM technique able to fabricate complex three-dimensional structures from ceramic or metallic powders. This vat polymerization method uses ultraviolet (UV) light to harden or cure a photopolymer resin. Meanwhile, a platform moves upward or downward after each new layer of the 3D-printed object is cured (Chua et al. 2017; Zheng et al. 2012). The DLP method is divided into three steps: (1) printing the 3D model into the required shape; (2) debinding, to remove the polymeric binder; and (3) sintering as a final step aimed at full consolidation. There are certain features of DLP, which makes it incompatible with a lunar environment, such as scarcity and outgassing of the resin. A plausible scenario is to replace the conventional resin with a bio-inspired alternative to adapt this AM method to lunar infrastructure (Shiwei et al. 2020). Furthermore, the debinding step must be optimised for vacuum to prevent defect formation, which may occur when volatile products are unable to effectively escape the green body. This is more likely to occur in vacuum debinding than air debinding due to higher activation energy for binder degradation processes (Wright et al. 1989). Nonetheless, resin and debinding development is outside of the scope of this research.

In this study, DLP was performed with an Admaflex 130 machine using the EAC-1A powder. The original powder was sieved through a 30 μm sieve and the content of lunar regolith powder of the slurry was set to 41%. Rectangular bars were 3D-printed with a layer thickness of 50 μm and a depth of cure of 100 μm. Water debinding was performed for 1 day followed by debinding in a furnace. Debinding in the furnace involved slow heating in air with stops at 150, 300, 400, and 600 °C to obtain the optimal removal of the resin and to reduce the remaining carbon as much as possible. The bars were then sintered in a standard furnace in an air atmosphere. The first sintering temperature was set to 1050 °C and kept for 1 h, with a slow heating rate of 100 °C/h. An additional sintering run at 1075 °C was carried out to improve the sintering of the bars.

Printing and debinding were successfully performed in the DLP process. However, the standard sintering step required further optimization to obtain good densification. Spark plasma sintering was then introduced to optimise the sintering parameters.

Spark plasma sintering (SPS) is a manufacturing technique that utilises uniaxial pressure and pulsed or unpulsed DC or AC current to consolidate powders into the required shape (Munir et al. 2006). SPS has been previously studied as a technique to

consolidate lunar regolith simulants, metal powders, or functionally graded materials (Zhang et al. 2021b; Long et al. 2013; Obadele et al. 2205; Radhamani et al. 2020; Tokita 2003). This study used a spark plasma sintering machine (SPS, FCT Group, Germany) operated under a vacuum and a 20 mm graphite die with graphite punches. With this new sintering technique, the tool and the component are directly heated by DC current pulses to reduce cycle times to a few minutes. During SPS a direct pulsed current of 1000 A, voltage of 6 V and pulse on/off 15:5 ms was applied. A pyrometer for process temperature regulation was focused on the inside of the top punch of the die. A 0.2 mm thick graphite foil was used to avoid adhesion and reaction between the powders and the graphite mould. Besides this foil, boron nitride spray was applied to reduce carbon diffusion into the sample. For this work, 4 mm high samples were pre-pressed to 10 kN before being set into the SPS machine.

Different sintering experiments were performed to identify which process parameters are relevant for EAC-1A and the metallic powders, see Tables 4.3 and 4.4. These values were identified in a two-step experiments in which metal and lunar regolith were sintered separately. Then, the optimal process parameters were selected as final values for a one-step experiment in which both materials were sintered under the same parameters to form the gradient (Table 4.9).

First, EAC-1A was sintered under the optimal parameters (1050°C, 80 MPa, milled powder), then Ti_6Al_4V was sintered at 1050°C, under 50 MPa with a holding time of 10 min. The optimal process parameters for stainless steel 316L were found to be 1100°C, 50 MPa, and a holding time of 20 min. The steel parameters were similar to those used for full sintering of crushed EAC-1A. The resulting parameters were then applied to another two-step experiment. The first step involved sintering of stainless steel in a layer under optimal parameters, followed by sintering of lunar regolith under its optimal conditions. Second, both layers were sintered under either optimal parameters for lunar regolith or 316L.

Table 4.3 Process parameters used for Spark Plasma Sintering of lunar regolith

No	Lunar regolith simulant	Sintering temperature (°C)	Pressure (MPa)	Holding time (min)	Maximum particle size (μm)
1	LHS-1	900	80	10	200
2	LHS-1	975	80	20	100
3	LHS-1	975	80	20	50
4	LHS-1	1025	80	20	50
5	LHS-1	1050	80	20	50
6	LHS-1	1075	80	20	50
7	LMS-1	1050	80	20	50
8	EAC-1A	1050	80	20	22
9	EAC-1A	1050	80	20	50
10	EAC-1A	1050	80	20	100

Table 4.4 Process parameters used for spark plasma sintering of metallic powders

Material	Sintering temperature (°C)	Pressure (MPa)	Holding time (min)	Maximum particle size (μm)
Stainless steel 316L	1050	50	10	30
	1050	50	20	30
	1100	50	20	30
Ti_6Al_4V	1000	50	10	45
	1050	50	10	45

4.2.3 Microstructural and Morphological Characterisation

XRD analysis was performed to determine the phases in the original powders and in the consolidated samples. The analysis was performed with a Bruker D8 Advance diffractometer using Cu K-alpha radiation. The step size used was 0.033° 2θ with 45 kV and 40 mA current in a 2θ range of 10–100°. The samples were ground with SiC 180 to remove the remaining graphite foil and to enable XRD analysis.

The density of the samples was measured based on Archimedes' principle. The samples were cleaned with isopropanol, dried, and then weighed dry and immersed in distilled water. Three density measurements were taken per sample type and the mean and standard deviation were calculated to give an accuracy range. Spark plasma sintered samples were discs of 20 mm diameter and 4 mm thickness. The specimens were cut into 2 half-discs, then embedded into a conductive resin, ground (SiC 80, 180, 320, 800, 1200, and 2000) and polished (MD Mol 3 μm and MD Nap 1 μm). Optical microscopy (Olympus BX60M) and scanning electron microscopy (SEM) in both secondary and backscattered modes were used for microstructural characterisation. Average porosity level and average relative sintered thickness were determined based on optical images. Porosity measurements were taken three times at 5 different locations; accuracy ranges were also taken based on the standard deviation. Energy dispersive spectroscopy (EDS) was performed to determine local composition and elemental distribution in the bulk and interface layers. Thermocalc® calculations were performed to determine the phases formed at the interface of FGM based on EDS results. Microhardness measurements were carried out using an automated Vickers hardness machine, Dura Scan (Struers). A load of 0.3 kgf (HV0.3) was used to measure the hardness of the lunar regolith sintered samples. It was observed that a higher load level results in severe cracking. For the metallic sintered samples, a load of 0.5 kgf (HV0.5) was used to measure their hardness. The hardness was measured at multiple locations on each sample and the average and standard deviation were calculated.

4.3 Results and Discussion

4.3.1 Consolidation of Lunar Regolith

Digital Light Processing (DLP)

Figure 4.5 shows lunar regolith (EAC-1A) printed samples with a layer thickness of 50 μm. Four bars were successfully printed with a height and width of 5 mm and a length of 100 mm. The debinding step was successful and the bars remained in their shape after being heat treated. The colour of the samples after debinding was the same as the initial powder; hence no significant change of the composition of the powder should have occurred.

It can thus be concluded that printing and debinding DLP steps can be performed without significant change in chemistry. After standard (in-air) sintering, the samples showed rather poor sintering characteristics: the bars did not keep their shape and cracked into small pieces. The sintered samples also changed in colour, to a light red. A similar colour change was also noticed by Liu et al., who found it to be associated with the transformation of Fe^{2+} to Fe^{3+} via oxidation reactions (Liu et al. 2019). Hence, standard in-air sintering is not suitable for this material and further optimization of the sintering step is required.

The microstructure of the samples showed poor sintering between particles (see Fig. 4.6a). However, the structure also shows larger particles surrounded by smaller particles, which would be beneficial for sintering as smaller particles can close the voids between coarser ones, resulting in better packing and densification. Furthermore, as shown in Fig. 4.6b, some particles coalesced and exhibited necking. This partial necking indicates that EAC-1A can be sintered with digital light processing (DLP). However, the sintering process requires further optimization, which is the scope of the follow-up sections.

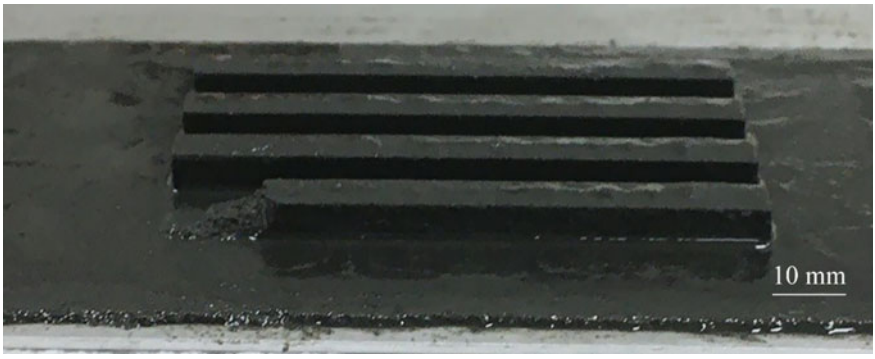

Fig. 4.5 DLP printed bars made out of lunar regolith EAC-1A

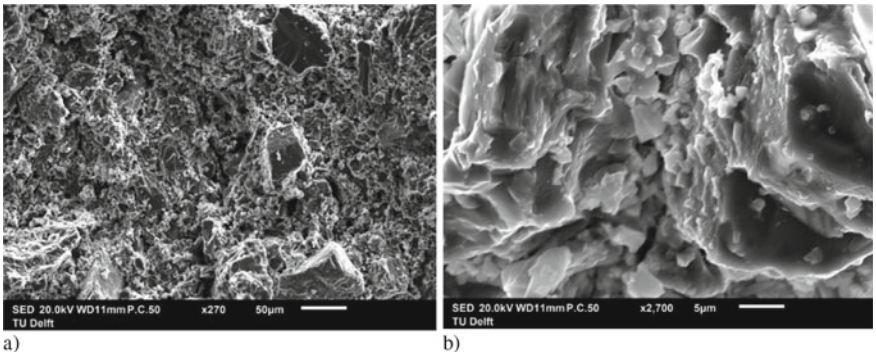

Fig. 4.6 SEM images of DLP samples sintered under standard in-air conditions: **a** low and **b** high magnifications

Spark Plasma Sintering (SPS)

SPS is proposed as a follow-up to DLP to increase densification of the lunar regolith. A number of experiments were performed using SPS techniques to optimise the technique. The results were analysed with respect to the sintering temperature, initial powder particle size, and different compositions in the lunar regolith powders.

Effect of SPS temperature

Table 4.5 shows the effect of SPS temperature on density and hardness. As can be seen, SPS significantly increases the density and hardness while reducing the porosity of lunar regolith simulant samples. The density was found to increase with the sintering temperature, with the maximum density of 2.704 ± 0.025 g.cm^{-3} achieved for the sample sintered at 1075 °C. It should be noted that sintering at 1075 °C led to partial melting. Due to partial melting the material spilled out of the sintering crucible and resulted in a non-stable process. It is therefore advisable to keep the sintering temperature below 1075 °C.

The microstructure of the samples was studied with SEM/EDS and their phases were determined with XRD (Figs. 4.7 and 4.8). Three main phases were present in the samples at all sintering temperatures: an augite light grey phase $Ca(Mg,Fe,Al)(Si,Al)_2O_6$, a sodian anorthite dark grey phase $(Ca,Na)(Si,Al)_4O_8$, and a white phase corresponding to an iron titanium oxide (Fig. 4.7). The sodian anorthite could have transformed to augite during the SPS experiment. The augite is often found

Table 4.5 Density and Vickers hardness of SPS sintered lunar regolith (LHS) samples

SPS temperature (°C)	Density (g/cm^3)	Porosity (%)	Hardness $HV_{0.3}$
1025	2.532 ± 0.046	23.7 ± 5.4	443 ± 56
1050	2.616 ± 0.060	21.0 ± 5.5	725 ± 77
1075	2.704 ± 0.025	11.7 ± 3.3	743 ± 142

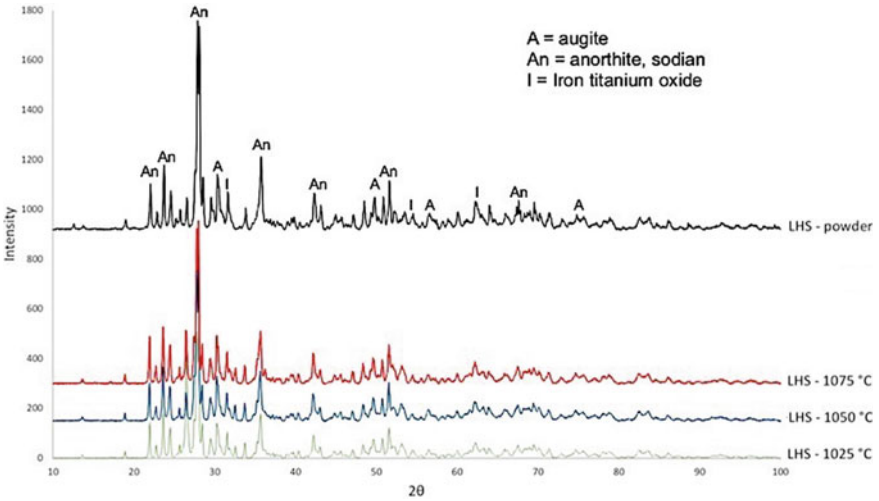

Fig. 4.7 XRD patterns of LHS sintered samples as compared to the LHS as-received powder

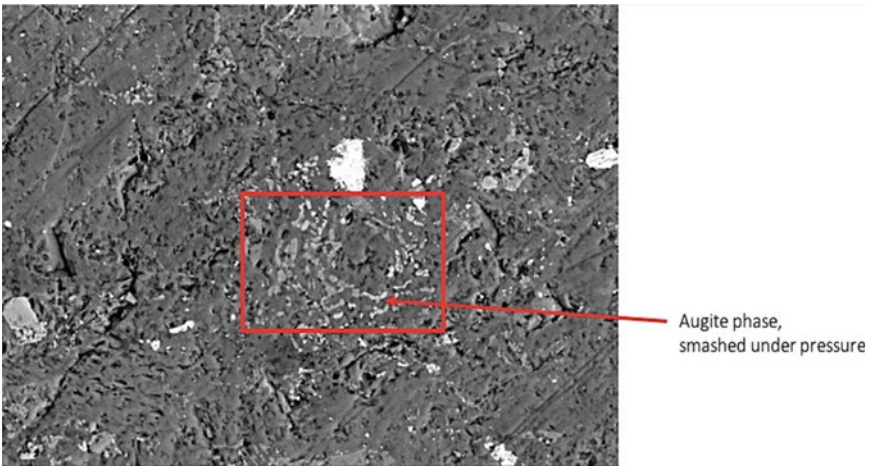

Fig. 4.8 Microstructure of the sintered LHS sample (at 1050 °C and 80 MPa)

in the form of "smashed" particles within the anorthite phase, as shown in Fig. 4.8. This microstructure could be due to the pressure applied during the SPS process. The partially dissolved anorthite can be pushed between the smashed augite particles by applying external pressure. Anorthite has a lower melting point and a lower modulus than augite: anorthite is thus more prone to plastic deformation under the applied pressure and can fill the gaps between the smashed augite particles (Zhang et al. 2019b). This specific microstructure was observed for all sintering temperatures.

The XRD patterns for the three different sintering temperatures were very similar: all samples exhibited the same diffraction peaks and were thus composed of the same minerals. This is in accordance with the SEM images, with the same three phases distinguished: augite, sodian anorthite, and iron titanium oxide. The compositions of the sintered samples are very similar to the composition of the powder as it was received.

Carbon was detected using EDS only on the outer part of the samples. This carbon originates from the graphite foil used to prevent the powder from sticking to the mould during SPS. Boron nitride was sprayed on the graphite foil to avoid this diffusion, but a small portion of carbon can still diffuse into the samples. Carbon diffusion is a thermally activated process. It increases when using higher sintering temperatures and higher pressure. Carbon only penetrates over a small layer of the sample and this layer can be removed by mechanical polishing. Viewed using EDS, the carbon was homogeneously present and had not formed any carbides.

Furthermore, the Vickers hardness also increased with the temperature. A significant increase was observed between the sintering temperatures of 1025 and 1050 °C. The hardness measurement is in accordance with the microstructure of the sintered samples. The high standard deviation is related to the different phases present in the specimens and the respective position of the measurement.

Effect of particle size

In order to evaluate the effect of particle size, EAC regolith samples with sieved powders of maximum particle size 22, 50, and 100 μm were sintered at an optimal temperature of 1050 °C and 80 MPa.

As can be seen in Table 4.6, samples with smaller particle size show higher densification. Moreover, the standard deviation is higher for samples with coarser particles, which indicates that the microstructure is more heterogeneous. It should also be noted that more macro-pores were observed in the coarser 100 μm sample. The presence of very coarse particles thus prevents good packing in the powder sample. The sample with the smallest initial particle size is the only sample that showed high vertical densification.

The higher densification of samples with finer powders can be related to several densification mechanisms: rearrangement of the particles, formation and growth of the sintering necks between the particles, and plastic deformation and densification (Cheng et al. 2017). The smaller the particle size, the higher the surface energy driving force, given in Eq. 4.1. The powder sintering is enhanced by the higher

Table 4.6 Density, Porosity, and Vickers hardness of lunar regolith (EAC) samples SPS sintered at 1050 °C temperature and 80 MPa pressure with different particle sizes

Particle size (μm)	Density (g/cm^3)	Porosity (%)	Hardness $HV_{0.3}$
<22	3.040 ± 0.046	4.3 ± 2.1	722 ± 35
<50	2.831 ± 0.077	15.5 ± 6.2	752 ± 74
<100	2.795 ± 0.078	21.4 ± 4.6	657 ± 46

driving force. This causes the migration of particles and increases the contact area between particles.

$$\Delta E = E_p - E_d \approx \gamma_{sv} W_m S_p \tag{4.1}$$

$$S_p \propto 1/R \tag{4.2}$$

Equations 4.1 and 4.2 show the relationship between the powder properties and the driving force for sintering. ΔE is the intrinsic driving force, E_p is the surface energy of the powder before sintering, E_d is the surface energy of powder after sintering, γ_{sv} (J/m^2) is the solid–gas surface energy, W_m (g/mol) is the molar mass of material, S_p (cm^2/g) is the specific surface area of powder, and R is the radius of the particle.

The tensile stress of the sintering necks increases with decreasing particle size, and the strength of the sintering necks is higher between smaller particles. Only the use of crushed EAC-1A powder (with resulting 22 μm particles) led to a fully dense sample (Fig. 4.9c). In the case of SPS, the particle surface is heated to higher temperatures compared to the particle core due to spark discharge in the voids. The surface-to-volume ratio of smaller particles is bigger than for coarse particles. The amount of the powder subjected to high temperatures is higher in the case of smaller particles, which leads to more effective densification. XRD patterns (Fig. 4.10) showed no significant differences between the samples consolidated with different particle sizes. The primary identified phases were plagioclase, pyroxenes (augite and diopside), and iron titanium oxide. The composition of the sintered samples is close to the composition of the initial powder.

The hardness of the sample with coarse particles is lower than for the other samples. The higher hardness for the sample with a maximum particle size of 50 μm is associated with a higher standard deviation due to the different hardness of the particles. Thus, the hardness of the 22 μm sample and the 50 μm sample are comparable. The hardness does not increase with powder milling as the phase composition remains similar, yet more homogeneously distributed.

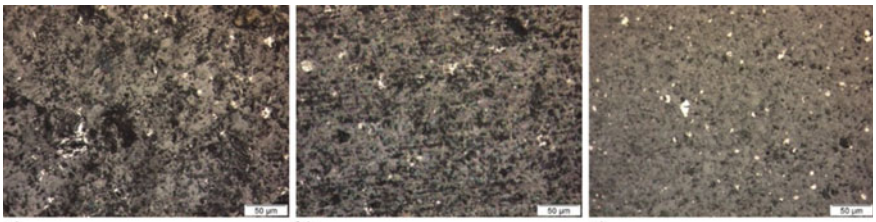

Fig. 4.9 Optical microscopy images of EAC-1A sintered samples with **a** 100 μm maximum particle size; **b** 50 μm maximum particle size; **c** 22 μm maximum particle size

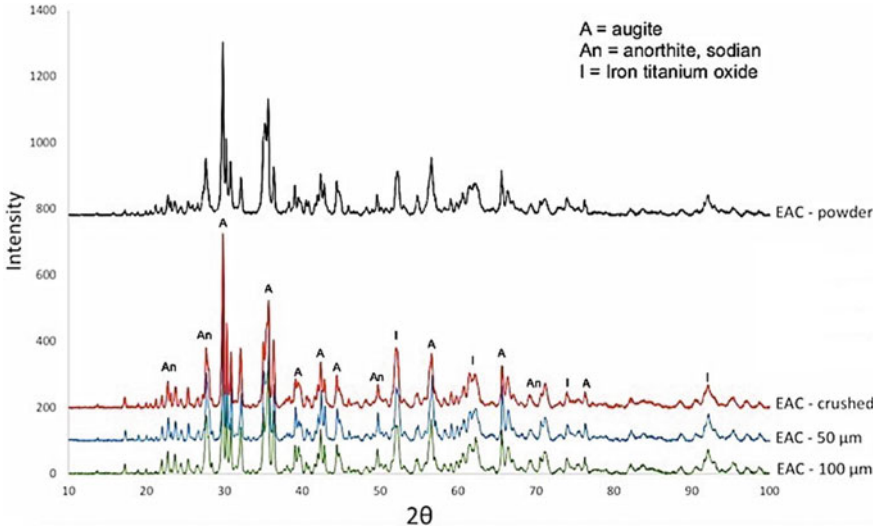

Fig. 4.10 XRD patterns for SPS samples with different particle sizes as compared with as-received powder

Effect of powder composition

In order to evaluate the effect of regolith simulants and their composition, the LHS-1, EAC-1A, and LMS-1 powders were spark plasma sintered at the previously determined optimal conditions of 1050 °C, 80 MPa pressure, and maximum particle size of 50 µm with a holding time of 20 min.

Table 4.7 shows that all three simulants result in a similar densification level and none of the powders melted under these sintering conditions (1050 °C, 80 MPa). The EAC-1A and LMS-1 samples displayed higher densification than the LHS-1 samples. It should however be noted that a thicker layer of fully dense material was measured for the LHS-1 sample. This indicates that the average porosity is lower for LMS-1 and EAC-1A, but LHS-1 has a more heterogeneous porosity with a highly densified part. All three simulants were found to be composed of the same oxides and minerals with comparable phase transition temperatures, and a similar expected behaviour for SPS.

Table 4.7 Density and Vickers hardness of SLS samples of different regolith simulants (max. particle size 50 µm)

Lunar regolith simulant type	Density (g/cm^3)	Porosity (%)	Hardness $HV_{0.3}$
LHS-1	2.616 ± 0.060	21.0 ± 5.5	725 ± 77
EAC-1A	2.831 ± 0.077	15.5 ± 6.2	752 ± 74
LMS-1	2.817 ± 0.083	21.6 ± 7.7	732 ± 167

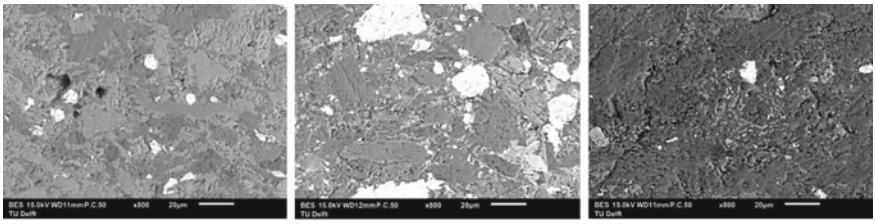

Fig. 4.11 SEM images of SPS samples for 3 different lunar regolith simulants: **a** EAC-1A, **b** LMS-1 and **c** LHS-1

The Vickers hardness of the samples was also not affected by the differences in simulant composition (Table 4.7). As LMS has more iron titanium oxide phases, the standard deviation could be influenced by these phases' presence at some material locations.

The microstructures of the sintered samples were also comparable and dense, with three main phases: augite, sodian anorthite, and iron titanium oxide. The LMS-1 samples showed a higher content of iron titanium oxide and coarser particles than the LHS-1 and EAC-1A samples (see white phases in Fig. 4.11b).

4.3.2 Consolidation of Metallic Powder

Consolidation of lunar regolith and metallic alloys has to be understood and optimised in order to develop a functionally graded multimaterial. The previous sections reviewed the consolidation of lunar regolith and the parameters influencing it. In this section, SPS consolidation of stainless steel and Ti_6Al_4V will be addressed.

Table 4.8 shows the optimization of SPS parameters based on density and hardness. As can be seen, increasing the sintering temperature increases the density and hardness of stainless steel. The density decrease is relatively low with increased holding time, although other authors observed the opposite trend (Marnier et al. 2014). In our study, the lower density could be due to poor rearrangement of the particles during sintering, preventing the pores from closing. The different balance between open pores and closed pores may also play a role, as the Archimedes measurements only take into account the open pores. However, when porosity is measured using optical techniques, the porosity reduces with increasing temperature.

All Ti_6Al_4V samples showed good densification and almost zero porosity. The applied uniaxial pressure of 50 MPa helps to rearrange the particles, breaking the agglomerates and inducing plastic deformation at high temperatures. The Joule heating effect derived from the pulsed current is another important densification mechanism. The current can flow through the highly conductive powdered sample, heating up the particles, especially on the particle surfaces. The temperature is thus

Table 4.8 Density and Vickers hardness of sintered stainless steel and Ti_6Al_4V (under 50 MPa pressure)

Material	Temperature / Holding time	Density (g/cm^3)	Porosity (%)	Hardness $HV_{0.5}$
Stainless steel 316	1050 °C/10 min	7.642 ± 0.046	3 ± 1.2	158 ± 5
	1050 °C/20 min	7.556 ± 0.015	1.4 ± 0.4	164 ± 6
	1100 °C/20 min	7.834 ± 0.010	0.9 ± 0.3	191 ± 5
Ti_6Al_4V	1000 °C/10 min	4.391 ± 0.018	1.2 ± 0.5	322 ± 11
	1050 °C/10 min	4.389 ± 0.006	0.7 ± 0.2	341 ± 23

higher at the contact point between particles. Diffusion thus increases and leads to higher and easier densification (Crosby et al. 2014).

Table 4.8 shows that the hardness for both alloys increased with rising sintering temperature. The hardness of samples sintered at 1050 °C is in the order of the hardness of the cast annealed 316 alloys (Rodrigues et al. 2021). The samples sintered at 1100 °C show a much higher hardness. The hardness was homogeneous across the whole sample and the standard deviation is relatively small for all samples, indicating that the microstructure and composition are also likely homogeneous. SEM analysis revealed a homogeneous microstructure for all samples and did not show any precipitates. Some nano-precipitates could be present, such as carbides due to carbon diffusion. However, they are not visible at the magnification used. Some authors reported the presence of carbides on grain boundaries (Marnier et al. 2014). Nevertheless, these carbides were found only on the thin edges of the samples.

The Vickers hardness for Ti_6Al_4V was found to be 341 $HV_{0.5}$ for the samples sintered at 1050 °C, compared to 322 $HV_{0.5}$ for the sample sintered at 1000 °C. These values are in the order of the Vickers hardness for Ti_6Al_4V cast alloys (Poondla et al. 2009).

The XRD results in Fig. 4.12 reveal only austenite phases present in all 316L samples. This fully austenitic microstructure was also observed by Keller et al. (2016).

For Ti_6Al_4V alloys, the elements Ti, Al, and V were found to be evenly distributed, and no precipitates formed during the sintering process. The XRD results in Fig. 4.13 show that the same phases form at two different sintering temperatures. The α-Ti phase is present as in the as-received powder, but a second phase is detected for both samples: $Ti_{0.8}V_{0.2}$, which is a β-Ti structure.

Microstructural analysis revealed the presence of clusters of grains elongated in the same direction. Recrystallization is not hindered by the presence of intermetallic at the grain boundaries or by interstitial solute atoms, as shown by Long et al. (2013).

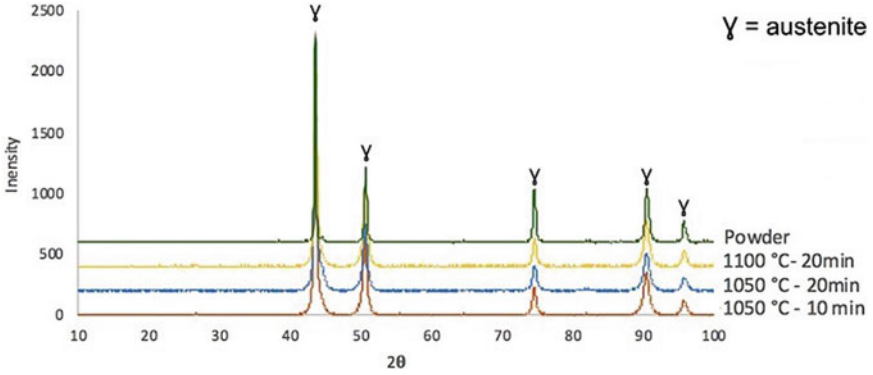

Fig. 4.12 XRD of SPSed stainless steel 316 samples and of as-received powder

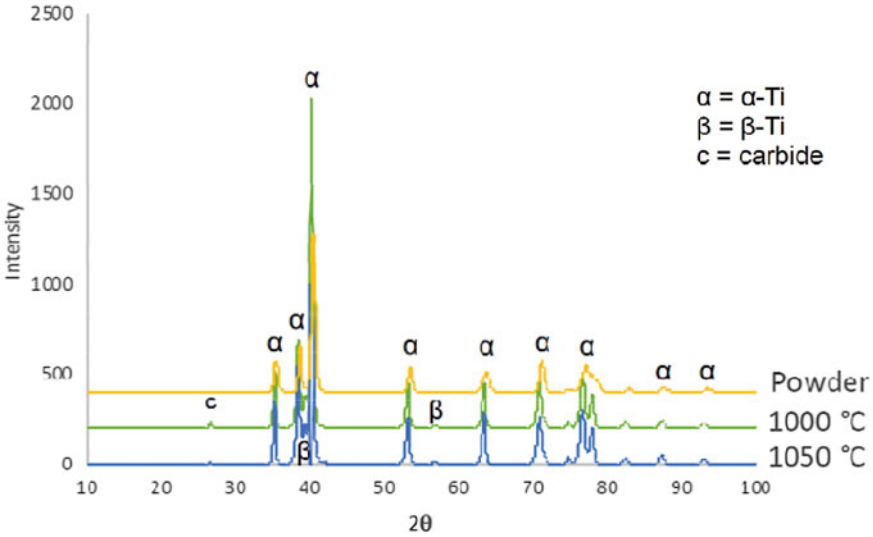

Fig. 4.13 XRD patterns of sintered Ti_6Al_4V and as-received powder

4.3.3 Consolidation of Functionally Graded Multimaterial (FGM)

The optimised parameters for FGM samples are based on the sintering results from regolith simulant and the individual metallic powders. The optimal SPS parameters for each material are displayed in Table 4.9.

Table 4.9 Optimal parameters for SPS of FGM based on lunar regolith simulant, stainless steel and titanium alloy

Material	Sintering temperature (°C)	Pressure (MPa)	Holding time (min)	Maximum particle size (μm)
Lunar regolith simulant EAC-1A	1050	80	20	22
Stainless steel 316L	1100	50	20	30
Ti_6Al_4V	1050	50	10	45

FGM Based on Lunar Regolith and Stainless Steel

The sintering was initially performed in one step by combining both lunar regolith (EAC-1A) and 316L green bodies. The experiment resulted in an inconsistent FGM and interfacial cracking. The one-step sintering at 1100 °C under 50 MPa completely melted the lunar regolith simulant, which was squeezed out of the SPS mould. The surface of the metallic part did not show any remnants of the lunar regolith. This experiment highlights that sintering at 1100 °C under 50 MPa is not suitable for the FGM lunar regolith simulant.

When sintering both powders at 1050 °C under 50 MPa, the FGM did not keep its shape and the EAC-1A and stainless-steel layers did not bond. Both layers exhibited cracks and porosity at the FGM interface, see Fig. 4.14. Thus, pressure of 50 MPa proved too low to allow for good sintering of the two powders. A minimal pressure of 80 MPa seemed to be required to sinter the lunar regolith, and a higher pressure may be required to allow for interfacial sintering.

Therefore, a two-step sintering was introduced and proved to be more successful. The thin layer of EAC-1A remained in contact with the metal. However, the FGM fractured within the lunar regolith layer upon removal from the SPS mould. This might be caused by the thermal expansion coefficient of stainless steel 316, which is twice as high as the lunar regolith (Ray et al. 2010). This mismatch in thermal properties induces thermal stresses during SPS cooling. These stresses can explain why

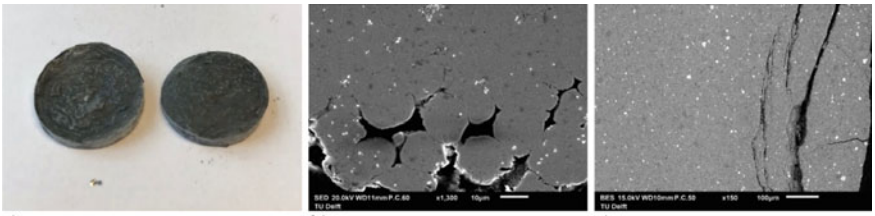

Fig. 4.14 **a** FGM 316/EAC after sintering at 1050 °C. SEM images of the interface between the two materials: **b** SS 316L and **c** EAC-1A

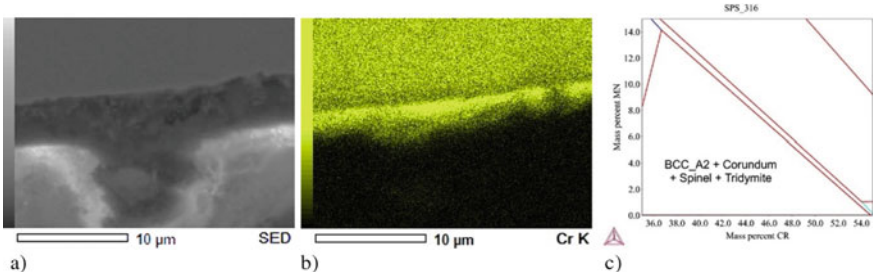

Fig. 4.15 **a** SEM image of interface of FGM 316/EAC, **b** EDS map of Cr at the interface of FGM 316/EAC and **c** Thermocalc graph for Cr diffusion

the FGMs cracked post-sintering. However, the interface between the two dissimilar materials remained intact. SEM images revealed the presence of a grey phase at the interface, featuring higher chromium concentration than in the inner layers (Fig. 4.15a). Chromium tends to diffuse from the stainless steel to the interface and form a high-content Cr phase; according to Thermocalc® calculations and composition from EDS, this is likely to be a BCC-A2 phase (Fig. 4.15b, c). Figure 4.16 shows the 316L/EAC functionally graded multimaterial hardness profile. The interface has a hardness much closer to the metallic alloy and does not exhibit a gradual transition, which is preferred for FGMs. Each hardness value was averaged based on 10 measurements for each location. Since the change in hardness between the interface and the lunar regolith is relatively large, it could explain the poor sintering properties of this type of FGM.

FGM Based on Lunar Regolith and Ti_6Al_4V Alloy

Ti_6Al_4V is the second alloy, selected for its good compatibility with lunar regolith. The produced FGM samples (Fig. 4.17) did not show any fractures, cracking, or interfacial porosity, which were characteristic of the previous 316L/EAC FGM. As shown in Fig. 4.17b, white particles, identified as titanium oxide, are present at the interface between the lunar regolith and Ti_6Al_4V. Moreover, EDS measurements reveal potential segregation of silicon at the interface (Fig. 4.18b), which forms the phase HCP_A3 (Ti_xSi_y) according to Thermocalc® calculations (Fig. 4.18c).

The Vickers hardness profile of this FGM shows a gradual transition from one material to another at the interface (Fig. 4.16). The hardness of the interface is close to the hardness of the lunar regolith. The coefficient of thermal expansion of Ti_6Al_4V and lunar regolith simulant is very close, about 8×10^{-6} K^{-1} for both materials (Karami, et al. 2020; Ray et al. 2010; Yakout et al. 2020). The similar coefficients help to prevent high thermal stresses during sintering, especially during the cooling stage.

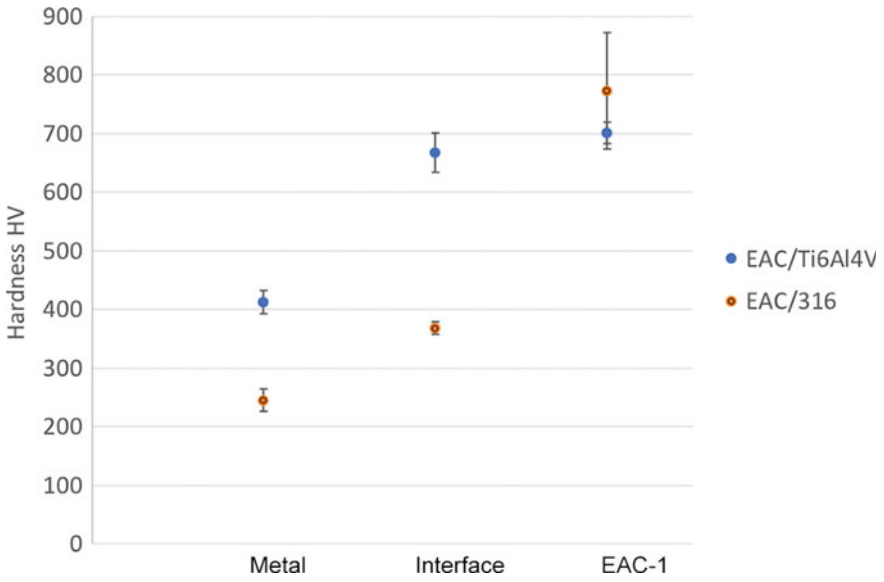

Fig. 4.16 Vickers hardness profile of the functionally graded multimaterials

Fig. 4.17 **a** FGM Ti_6Al_4V /EAC-1A after sintering in 2 steps and **b** SEM image of the interface between Ti_6Al_4V (light, below) and EAC-1A (dark, above)

4.4 Conclusions

This study investigated additive manufacturing and spark plasma sintering techniques to identify the feasibility of a functionally graded metallic-regolith. Initially, the lunar regolith simulants were additively manufactured and debinded using the digital light processing technique. Then, spark plasma sintering was applied and optimised using different sintering conditions, namely temperature, particle size, and composition. The same SPS approach was also applied to the metallic powders. Finally, the

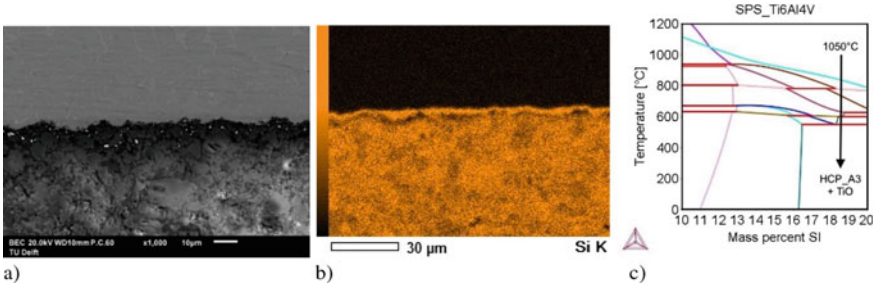

Fig. 4.18 **a** SEM image of the interface of FGM Ti_6Al_4V/EAC, **b** EDS of Si at the interface of FGM and Ti_6Al_4V, **c** Thermocalc graph for Ti_6Al_4V /EAC interface

optimal processing conditions were developed for the consolidation of functionally graded metallic-regolith concerning densification, microstructural, compositional, and microhardness characteristics.

The research identified that lunar regolith simulants could be successfully additively manufactured via a combination of digital light processing and spark plasma sintering at 1050 °C under 80 MPa (Table 4.10). For better densification, it is required to sieve or mill the powders to the 20–50 µm range before the fabrication process. Additionally, a higher pressure could be used to avoid the milling step. The composition of the sintered samples is similar to the powder composition of augite, sodian anorthite, and iron titanium oxides. Furthermore, increasing the temperature and reducing the particle size in this process has increased densification and Vickers microhardness. Metallic powders can be fully densified with SPS at relatively low temperatures and a pressure of 50 MPa. Both stainless steel and Ti_6Al_4V showed a homogeneous structure without precipitates or carbides. Therefore, with optimal SPS parameters, this study displays that FGMs can be fabricated. The most promising gradient has been the combination of lunar regolith and Ti_6Al_4V. The hardness profile showed a gradual transition between these two layers, while the interface is strong enough to avert cracking.

This FGM feasibility study displayed promising results in the additive manufacturing field of in-space resources. The DLP process holds a uniquely high potential for printing complex geometries. Further studies could investigate methods for high-pressure sintering of complex green bodies to make full use of the DLP potential for FGM manufacture. To adapt the DLP method for lunar infrastructure, the next step is to investigate compatible resins. The debinding step should be optimised for the lunar environment to prevent the charcoal formation and defects by tailoring powder morphology, resin, heating rate, and geometry. Moreover, the SPS technique would have to be modified to be employed on the Moon for large-scale production. This study showed the local melting of the powder at 1075 °C. Thus, laser-based additive manufacturing techniques could be investigated as a method for applying lunar regolith as a coating onto metallic surfaces to achieve better wear, corrosion, and thermal resistance.

Table 4.10 Advantages and limitations of functionally graded Ti_6Al_4V/EAC and 316L/EAC-1A

FGM	Process parameters	Advantages	Disadvantages
Ti_6Al_4V/EAC-1A	1050 °C, 50–80 MPa, 10 min, 22/45 μm particle size, DLP and SPS	• Strong interface • No fractures • No cracking • No interfacial porosity	• Requires a two-step sintering process • The powders require sieving to match the particle size
316L/EAC-1A	1050–1100 °C, 50–80 MPa, 20 min, 22/30 μm particle size, DLP and SPS	• Hardness similar to the alloy • Intact interface	• Requires a two-step sintering process • Mismatch in thermal properties results in cracking • The powders require sieving to match the particle size

Further investigation can also be considered for the mechanical properties of regolith-metallic graded multimaterial. Mainly, compressive strength, fracture toughness, and thermal fatigue behaviour are relevant properties to consider for lunar habitats and wear resistance for the coating applications of space components. Thermal and wear properties are likely to be improved over metallic substrate alone, whereby fracture resistance will be greater than regolith alone. Understanding these properties is a significant next step towards validating this method for lunar applications. Additionally, the combination of regolith with other metals in pure composition can be investigated. Pure aluminum, iron, and titanium powders are needed to determine optimal FGM manufacturing in conditions closer to a lunar scenario.

In-situ resource utilisation and advanced materials are essential for future space habitation on the Moon. To fabricate these habitats, high-mechanical performance materials are required. This study identified functionally graded multimaterials fit for extreme environments and can be manufactured with in-situ resources. A speculative future case scenario can apply this technique to lunar habitats. This habitat can be additive manufactured from a gradient from metal to regolith and tailored to respond to the harsh environmental conditions, see Fig. 4.19.

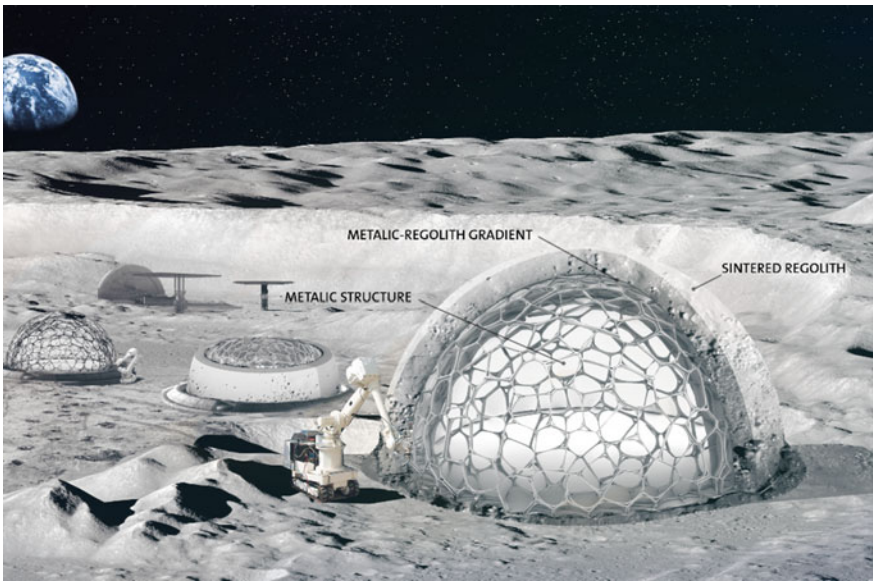

Fig. 4.19 Hypothetical additive manufacturing of functionally graded materials for a lunar habitat

Acknowledgements The authors would like to acknowledge the support of the European Space Agency (ESA) via the Ariadna 19-D-A-02 research funding. Furthermore, we would like to express gratitude to the ESA technicians at the European Space Research and Technology Centre (ESTEC), in particular to Advenit Makaya, Sarah Rodríguez Castillo, and Martina Meisnar, as well as Jaap Hooijmans at Admatec for his assistance in performing DLP.

References

Allen CC, Morris RV, McKay DS (1996) Oxygen extraction from lunar soils and pyroclastic glass. J Geophys Res E Planets 101(E11):26085–26095

Altun AA, Ertl F, Marechal M, Makaya A, Sgambati A, Schwentenwein M (2020) Additive manufacturing of lunar regolith structures. Open Ceram 5(September 2020):100058

Altun AA, Ertl F, Marechal M, Makaya A, Sgambati A, Schwentenwein M (2021) Additive manufacturing of lunar regolith structures. Open Ceram 5(December 2020):100058

ASTM F2792-12 (2012) Standard terminology for additive manufacturing technologies

Balla VK, Bandyopadhyay PP, Bose S, Bandyopadhyay A (2007) Compositionally graded yttria-stabilized zirconia coating on stainless steel using laser engineered net shaping (LENS^{TM}). Scr Mater 57(9):861–864

Balla VK, Roberson LB, O'Connor GW, Trigwell S, Bose S, Bandyopadhyay A (2012) First demonstration on direct laser fabrication of lunar regolith parts. Rapid Prototyp J 18(6):451–457

Benaroya H (2018) Building habitats on the moon: engineering approaches to lunar settlements. Springer

Benaroya H (2022) The evolution of lunar habitat concepts. Int J Sp Struct 37(3):187–195

Bever MB, Duwez PE (1972) Gradients in composite materials. Mater Sci Eng 10(C):1–8

Brown GM, Peckett A, Emeleus CH, Phillips R, Pinsent RH (1975) Petrology and mineralogy of Apollo 17 mare basalts. In: Lunar and planetary science conference proceedings, vol 6, pp 1–13
Buchanan C, Gardner L (2019) Metal 3D printing in construction: A review of methods, research, applications, opportunities and challenges. Eng Struct 180(March 2018):332–348
Cannon K (2019) Planetary simulant database. https://sciences.ucf.edu/class/exolithlab
Carloni D, Zhang G, Wu Y (2021) Transparent alumina ceramics fabricated by 3D printing and vacuum sintering. J Eur Ceram Soc 41(1):781–791
Cesaretti G, Dini E, De Kestelier X, Colla V, Pambaguian L (2014) Building components for an outpost on the lunar soil by means of a novel 3D printing technology. Acta Astronaut 93:430–450
Cheibas I, Laot M, Popovich VA, Rich B, Rodriguez Castillo S (2020) Additive manufacturing of functionally graded materials with in-situ resources. In: Aerospace Europe Conference (AEC 2020) (June):0–12
Cheibas I, Arnhof M, Rich B (2022) Basalt fiber composites for the robotic fabrication of a lunar habitat. In: 73rd International astronautical congress (IAC). Copyright by IAF, Paris
Cheng Y, Cui Z, Cheng L, Gong D, Wang W (2017) Effect of particle size on densification of pure magnesium during spark plasma sintering. Adv Powder Technol 28(4):1129–1135
Chua CK, Wong CH, Yeong WY (2017) Material characterization for additive manufacturing
Cordonier GJ et al (2021) Direct foam writing in microgravity. npj Microgravity 7(1):1–5
Crawford IA (2015) Lunar resources: a review. Prog Phys Geogr 39(2):137–167
Crosby K, Shaw LL, Estournes C, Chevallier G, Fliflet AW, Imam MA (2014) Enhancement in Ti-6Al-4V sintering via nanostructured powder and spark plasma sintering. Powder Metall 57(2):147–154
Dordlofva C, Törlind P (2020) Qualification challenges with additive manufacturing in space applications. In: 2017 Proceedings of the 28th annual international solid freeform fabrication symposium—an additive manufacturing conference SFF 2017, pp 2699–2712
Dou R, Tang W, Hu K, Wang L (2022) Ceramic paste for space stereolithography 3D printing technology in microgravity environment. J Eur Ceram Soc 42(9):3968–3975
Dronadula R, Benaroya H (2021) Hybrid lunar inflatable structure. Acta Astronaut 179(August 2020):42–55
Eckart P (1999) The lunar base handbook, p 850
Eckart P, Clarke AC, Schmitt HH (1999) Lunar base handbook, 2nd edition 2006, Publisher: McGraw-Hill Education
Edmunson J, Rickman DL (2012) A survey of geologic resources. In: Moon. Springer, pp 1–21
Ellery A (2022) Leveraging in situ resources for lunar base construction. Can J Civ Eng 49(5):657–674
Ellery A, Mellor I, Wanjara P, Conti M (2022) Metalysis fray farthing chen process as a strategic lunar in situ resource utilization technology. New Space 10(2):224–238. https://home.liebertpub.com/space
ESA. Brick 3D printed from moondust using focused sunlight. https://www.esa.int/ESA_Multimedia/Images/2017/03/Brick_3D_printed_from_moondust_using_focused_sunlight. Accessed 12 Mar 2023
Fateri M, Gebhardt A (2015) Process parameters development of selective laser melting of lunar regolith for on-site manufacturing applications. Int J Appl Ceram Technol 12(1):46–52
Fateri M, Pitikaris S, Sperl M (2019) Investigation on wetting and melting behavior of lunar regolith simulant for additive manufacturing application. Microgravity Sci Technol 31(2):161–167
Fateri M, Meurisse A, Sperl M, Consortium R (2017) Solar sintering for additive manufacturing on the moon. EPSC Abstr 11(2014)
Frank J, Spirkovska L, McCann R, Wang L, Pohlkamp K, Morin L (2013) Autonomous mission operations. In: IEEE aerospace conference proceeding 2013
Galjaard S, Hofman S, Perry N, Ren S (2015) Optimizing structural building elements in metal by using additive manufacturing. In: Proceedings of IASS annual symposia, international association for shell and spatial structures (IASS), no 2, pp 1–12

Gardner L, Kyvelou P, Herbert G, Buchanan C (2020) Testing and initial verification of the world's first metal 3D printed bridge. J Constr Steel Res 172

Geng Y et al (2021) Ti–6Al–4V microstructural functionally graded material by additive manufacturing: experiment and computational modelling. Mater Sci Eng A 823(May):141782

Gong F, Zhao J, Li Z, Sun J, Ni X, Hou G (2018) Design, fabrication and mechanical properties of multidimensional graded ceramic tool materials. Ceram Int 44(3):2941–2951

Goulas A, Friel RJ (2016) 3D printing with moondust. Rapid Prototyp J 22(6):864–870

Goulas A, Binner JGP, Harris RA, Friel RJ (2017) Assessing extraterrestrial regolith material simulants for in-situ resource utilisation based 3D printing. Appl Mater Today 6:54–61

Goulas A, Binner JGP, Engstrøm DS, Harris RA, Friel RJ (2019) Mechanical behaviour of additively manufactured lunar regolith simulant components. Proc Inst Mech Eng Part L J Mater Des Appl 233(8):1629–1644

Guisard Restivo TA et al (2019) Micrograded ceramic-metal composites. J Eur Ceram Soc

Heiken GH, Vaniman DT, French BM (1991) Lunar sourcebook-a user's guide to the moon. Research Supported by NASA, Cambridge, England, Cambridge University Press, 753 p (No individual items are abstract this volume)

Higgins M, Benaroya H (2020) Utilizing the analytical hierarchy process to determine the optimal lunar habitat configuration. Acta Astronaut 173(January):145–154

Howe AS, Sherwood B (2009) Out of this world: the new field of space architecture. American Institute of Aeronautics and Astronautics

Isachenkov M, Chugunov S, Akhatov I, Shishkovsky I (2021) Regolith-based additive manufacturing for sustainable development of lunar infrastructure—An overview. Acta Astronaut 180(January):650–678

Isachenkov M, Chugunov S, Akhatov I, Shishkovsky I (2021) Regolith-based additive manufacturing for sustainable development of lunar infrastructure—an overview. Acta Astronaut 180:650–678

Jin Q, Ren XP, Hou HL, Zhang YL, Qu HT (2018) In situ synthesis and structural design of Ti/TiC functionally graded materials. Mater Sci Forum 913:515–521

Kamaruzaman FF, Nuruzzaman DM, Ismail NM, Hamedon Z, Iqbal AKMA, Azhari A (2018) Microstructure and properties of aluminium-aluminium oxide graded composite materials. IOP Conf Ser Mater Sci Eng 319(1):0–6

Kanyilmaz A et al (2021) Role of metal 3D printing to increase quality and resource-efficiency in the construction sector. Addit Manuf 50(November):2022

Karami K et al (2020) Continuous and pulsed selective laser melting of Ti6Al4V lattice structures: effect of post-processing on microstructural anisotropy and fatigue behaviour. Addit Manuf 36(April):101433

Katz-demyanetz A, Popov VV, Kovalevsky A, Safranchik D (2019) Powder-bed additive manufacturing for aerospace application: techniques, metallic and metal/ceramic composite materials and trends 5

Keller C, Tabalaiev K, Marnier G, Noudem J, Sauvage X, Hug E (2016) Influence of spark plasma sintering conditions on the sintering and functional properties of an ultra-fine grained 316L stainless steel obtained from ball-milled powder. Mater Sci Eng A 665:125–134

Kennedy KJ (2002) The vernacular of space architecture. In: AIAA space architecture symposium (October), pp 1–15

Khoshnevis B et al (2005) Lunar contour crafting—a novel technique for ISRU-based habitat development. In: 43rd AIAA aerospace sciences meeting and exhibit (February), pp 7397–7409

Kim BH, Na YH (1995) Fabrication of fiber-reinforced porous ceramics of Al_2O_3-mullite and SiC-mullite systems. Ceram Int 21(6):381–384

Kim YJ, Ryu BH, Jin H, Lee J, Shin HS (2021) Microstructural, mechanical, and thermal properties of microwave-sintered KLS-1 lunar regolith simulant. Ceram Int 47(19):26891–26897

Kost PM et al (2021) Thermal properties of lunar regolith simulant melting specimen. Acta Astronaut 187(July):429–437

Labeaga-Martínez N, Sanjurjo-Rivo M, Díaz-Álvarez J, Martínez-Frías J (2017) Additive manufacturing for a moon village. Procedia Manuf 13:794–801
Lakhdar Y, Tuck C, Binner J, Terry A, Goodridge R (2021) Additive manufacturing of advanced ceramic materials. Prog Mater Sci 116:100736
Landis GA (2007) Materials refining on the Moon. Acta Astronaut 60(10–11):906–915
Li W, Lan D, Wang Y (2020) Exploration of direct-ink-write 3D printing in space: droplet dynamics and patterns formation in microgravity. Microgravity Sci Technol 32(5):935–940
Liao H, Zhu J, Chang S, Xue G, Pang J, Zhu H (2021) Lunar regolith—AlSi10Mg composite fabricated by selective laser melting. Vacuum 187(November 2020):110122
Licheri R, Orrù R, Sani E, Dell'Oro A, Cao G (2022) Spark plasma sintering and optical characterization of lunar regolith simulant. Acta Astronaut 201(January):164–171
Liu M et al (2019) Digital light processing of lunar regolith structures with high mechanical properties. Ceram Int 45(5):5829–5836
Lomax BA, Conti M, Khan N, Bennett NS, Ganin AY, Symes MD (2020) Proving the viability of an electrochemical process for the simultaneous extraction of oxygen and production of metal alloys from lunar regolith. Planet Space Sci 180(April 2019):104748
Long Y et al (2013) High-strength Ti-6Al-4V with ultrafine-grained structure fabricated by high energy ball milling and spark plasma sintering. Mater Sci Eng A 585:408–414
Marnier G, Keller C, Noudem J, Hug E (2014) Functional properties of a spark plasma sintered ultrafine-grained 316L steel. Mater Des 63:633–640
Maseko SW, Popoola API, Fayomi OSI (2018) Characterization of ceramic reinforced titanium matrix composites fabricated by spark plasma sintering for anti-ballistic applications. Def Technol 14(5):408–411
Mertens A et al (2014) Mechanical properties of alloy Ti-6Al-4V and of stainless steel 316L processed by selective laser melting: influence of out-of-equilibrium microstructures. Powder Metall 57(3):184–189
Meurisse A, Beltzung JC, Kolbe M, Cowley A, Sperl M (2017) Influence of mineral composition on sintering lunar regolith. J Aerosp Eng 30(4):04017014
Meurisse A, Makaya A, Willsch C, Sperl M (2018) Solar 3D printing of lunar regolith. Acta Astronaut 152(September):800–810
Mueller S, Taylor GJ, Phillips RJ (1988) Lunar composition: a geophysical and petrological synthesis. J Geophys Res Solid Earth 93(B6):6338–6352
Munir ZA, Anselmi-Tamburini U, Ohyanagi M (2006) The effect of electric field and pressure on the synthesis and consolidation of materials: a review of the spark plasma sintering method. J Mater Sci 41(3):763–777
MX3D (2021) Robotic 3D metal printing|WAAM
Naser MZ, Chehab AI (2018) Materials and design concepts for space-resilient structures. Prog Aerosp Sci 98(March):74–90
Neves JM, Ramanathan S, Suraneni P, Grugel R, Radlińska A (2020) Characterization, mechanical properties, and microstructural development of lunar regolith simulant-portland cement blended mixtures. Constr Build Mater 258(2020):1–10
Nunn Z, Smith S, Culton J (2022) Lunar resources in support of human interplanetary settlement and limitations. In: Space manufacturing and resources: earth and planetary exploration applications, pp 223–234
Obadele BA, Adesina OS, Oladijo OP, Ogunmuyiwa EN (2020) Fabrication of functionally graded 316L austenitic and 2205 duplex stainless steels by spark plasma sintering. J Alloys Compd 849
Papike JJ, Simon SB, Laul JC (1982) The lunar regolith: chemistry, mineralogy, and petrology. Rev Geophys 20(4):761–826
Pasha A, Rajaprakash BM (2021) Fabrication and mechanical properties of functionally graded materials: a review. Mater Today Proc (xxxx)
Pieters CM (1986) Composition of the lunar highland crust from near-infrared spectroscopy. Rev Geophys 24(3):557–578

Pilehvar S, Arnhof M, Pamies R, Valentini L, Kjøniksen AL (2020) Utilization of urea as an accessible superplasticizer on the moon for lunar geopolymer mixtures. J Clean Prod 247

Poondla N, Srivatsan TS, Patnaik A, Petraroli M (2009) A study of the microstructure and hardness of two titanium alloys: commercially pure and Ti–6Al–4V. J Alloys Compd 486(1–2):162–167

Popovich VA, Borisov EV, Heurtebise V, Riemslag T, Popovich AA, Sufiiarov VS (2018) Creep and thermomechanical fatigue of functionally graded inconel 718 produced by additive manufacturing. In: TMS 2018—147th annual meeting and exhibition, pp 85–97

Prettyman TH et al (2006) Elemental composition of the lunar surface: analysis of gamma ray spectroscopy data from Lunar Prospector. J Geophys Res Planets 111(E12)

Radhamani AV, Lau HC, Kamaraj M, Ramakrishna S (2020) Structural, mechanical and tribological investigations of CNT-316 stainless steel nanocomposites processed via spark plasma sintering. Tribol Int 152(March):106524

Rasera JN, Cilliers JJ, Lamamy JA, Hadler K (2020) The beneficiation of lunar regolith for space resource utilisation: a review. Planet Space Sci 186(October 2019):104879

Rattanachan S, Miyashita Y, Mutoh Y (2003) Microstructure and fracture toughness of a spark plasma sintered Al_2O_3-based composite with $BaTiO_3$ particulates. J Eur Ceram Soc 23(8):1269–1276

Ray CS, Reis ST, Sen S, O'Dell JS (2010) JSC-1A lunar soil simulant: characterization, glass formation, and selected glass properties. J Non Cryst Solids 356(44–49):2369–2374

Rodrigues TA et al (2021) Effect of heat treatments on 316 stainless steel parts fabricated by wire and arc additive manufacturing: microstructure and synchrotron X-ray diffraction analysis. Addit Manuf 48(PB):102428

Ruys AJ, Popov EB, Sun D, Russell JJ, Murray CCJ (2001) Functionally graded electrical/thermal ceramic systems. J Eur Ceram Soc 21(10–11):2025–2029

Sanders GB, Larson WE (2012) Progress made in lunar in situ resource utilization under NASA's exploration technology and development program. Earth Space 2012(281):457–478

Schleppi J, Gibbons J, Groetsch A, Buckman J, Cowley A, Bennett N (2019) Manufacture of glass and mirrors from lunar regolith simulant. J Mater Sci 54(5):3726–3747

Schlüter L, Cowley A (2020) Review of techniques for In-Situ oxygen extraction on the moon. Planet Space Sci 181(April 2019):104753

Shiwei N, Dritsas S, Fernandez JG (2020) Martian biolith: a bioinspired regolith composite for closed-loop extraterrestrial manufacturing. PLoS One 15(9 September):1–11

Sibille L, Carpenter P, Schlagheck R, French RA (2006) Lunar regolith simulant materials: recommendations for standardization, production, and usage

Smith C et al (2018) The European Space Agency Exploration Sample Analogue Collection (ESA2C) and curation facility-present and future. In: 42nd COSPAR Sci. Assem, vol 42, pp B4–B2

Srivastava M, Rathee S, Maheshwari S, Kundra TK (2019) Design and processing of functionally graded material: review and current status of research. In: 3D Printing and additive manufacturing technologies, Springer, pp 243–255

Suresh S, Mortensen A (1997) Functionally graded metals and metal-ceramic composites: part 2 Thermomechanical behaviour. Int Mater Rev 42(3):85–116

Taylor SR (1987) The unique lunar composition and its bearing on the origin of the Moon. Geochim Cosmochim Acta 51(5):1297–1309

Tokita M (2003) Large-size WC/Co functionally graded materials fabricated by spark plasma sintering (SPS) method. Mater Sci Forum 423–425:39–44

Wright JK, Evans JRG, Edirisinghe MJ (1989) Degradation of polyolefin blends used for ceramic injection molding. J Am Ceram Soc 72(10):1822–1828

Yakout M, Elbestawi MA, Veldhuis SC (2020) A study of the relationship between thermal expansion and residual stresses in selective laser melting of Ti-6Al-4V. J Manuf Process 52:181–192

Zhang B, Jaiswal P, Rai R, Nelaturi S (2018) Additive manufacturing of functionally graded material objects: a review. J Comput Inf Sci Eng 18(4):041002

Zhang T et al (2021a) Robotic drilling tests in simulated lunar regolith environment. J Field Robot 38(8):1011–1035

Zhang X et al (2021b) Spark plasma sintering of a lunar regolith simulant: effects of parameters on microstructure evolution, phase transformation, and mechanical properties. Ceram Int 47(4):5209–5220

Zhang X et al (2019a) Microstructure evolution during spark plasma sintering of FJS-1 lunar soil simulant. J Am Ceram Soc (April 2019):899–911

Zhang X et al (2019b) Microstructure evolution during spark plasma sintering of FJS-1 lunar soil simulant. J Am Ceram Soc (September):1–13

Zheng X et al (2012) Design and optimization of a light-emitting diode projection micro-stereolithography three-dimensional manufacturing system. Rev Sci Instrum 83(12)